Research Article | Vol. 28, No. 23 / 9 November 2020 / Optics Express 34111

Optics EXPRESS

Low-loss and ultra-broadband silicon nitride angled MMI polarization splitter/combiner

Ramesh Kudalippalliyalil,[1,2,*] Thomas E. Murphy,[1] and Karen E. Grutter[2]

[1] *Institute for Research in Electronics & Applied Physics, University of Maryland, College Park, MD 20742, USA*
[2] *Laboratory for Physical Sciences, College Park, MD 20740, USA*
[*] *rameshk@umd.edu*

Abstract: The property of self-imaging combined with the polarization birefringence of the angled multimode waveguide is used to design a silicon nitride (SiN) polarization splitter (PS) at $\lambda \sim 1550$ nm. The demonstrated PS on a 450 nm thick SiN device layer (with 2.5 µm cladding oxide) has a footprint of 80 µm×13 µm and exhibits nearly wavelength independent performance over the C+L bands. Also, the device can be configured as a polarization combiner (PC) in reverse direction with similar bandwidth and performance. The measured crosstalk (CT) and insertion loss (IL) are respectively <-18 dB (<-20 dB) and ~0.7 dB (~0.8 dB) for TE (TM) polarization over the measurement wavelength range of 1525 nm $\leq \lambda \leq$ 1625 nm. The measured device parameter variations suggest some tolerance to fabrication variations. Such a device is a good candidate for a photonics integrated chip (PIC) foundry-compatible, SiN PS.

1. Introduction

Silicon photonics offers high efficiency and low cost technological solutions for the large scale monolithic integration of complex photonics functions onto a photonic integrated circuit (PIC) [1–4]. Within silicon photonics, both silicon and silicon nitride (Si_3N_4 or SiN) are widely-used photonic materials that can leverage existing CMOS foundry resources [5–7]. Silicon-on-insulator (SOI) devices are most extensively used for high density integration of both passive and active PICs. However, the tight fabrication tolerances, strong polarization dependence, high thermal sensitivity, large waveguide dispersion, and nonlinear absorption of silicon wire waveguides impose limits on their applicability. In contrast, SiN on silica (SiO_2) has a wider transparency range, lower thermo-optic coefficient, and greater fabrication tolerance than SOI waveguides, making SiN a more suitable platform for some passive devices. Furthermore, SiN devices can be easily co-integrated with SOI devices using low pressure chemical vapor deposition (LPCVD) or plasma enhanced chemical vapor deposition (PECVD) [7]. These characteristics have been used to make various linear and nonlinear photonic devices with low IL and broad bandwidth (visible-near infrared-mid infrared) [8–12].

PICs in both materials are inherently sensitive to polarization due to the geometric birefringence of photonic waveguides. The different propagation constants of transverse electric (TE) and transverse magnetic (TM) modes causes polarization mode dispersion, polarization-dependent loss, and polarization-dependent spectral response [13]. Consequently, polarization management is of great importance in PICs. Various on-chip polarization management schemes have been proposed [14–17]. A square waveguide core may be used for polarization-independent photonic circuits [18], but this requires stringent fabrication tolerances, as fabrication errors of a couple of nanometers or material strain in device geometry result in uncontrolled birefringence. Polarization diversity is the most reliable polarization management approach, where input light with arbitrary polarization is first split into two orthogonal components (TE and TM) and one polarization is then rotated so that the two spatially separated, but co-polarized channels can be independently

#405188 https://doi.org/10.1364/OE.405188
Journal © 2020 Received 13 Aug 2020; revised 6 Oct 2020; accepted 7 Oct 2020; published 27 Oct 2020

Optics EXPRESS

processed. The resulting outputs can optionally be recombined, using a similar rotator/splitter in reverse. [19–21]. Such a scheme is realized using a polarization splitter-rotator (PSR) or a polarization splitter (PS) followed by a polarization rotator (PR). Great efforts have been made in realizing these devices in different material platforms, including SOI, SiN-on-SOI and SiN. PSRs are designed either based on a mode coupling approach or a mode evolution approach. Mode coupling requires critical phase matching, making it inherently fabrication-sensitive and wavelength-dependent [22–25]. Mode-evolution-based PSRs utilize a hybrid-mode waveguide approach and hence cannot be fabricated in a single-step process [26–29].

Independent PSs provide more flexibility to use both the polarizations for specific applications [30]. Asymmetric directional couplers (DCs) [31], bent DCs [32,33], Mach-Zehnder interferometers (MZIs) [34,35] and multimode interferometers (MMIs) [36] are the most commonly used splitting elements. For maximum performance, DCs and DC-based MZI devices require precise control over critical dimensions, especially the gap width and length of the DC. In contrast, conventional MMI-based PSs have greater fabrication tolerance, but they exhibit significant insertion loss (IL) and crosstalk (CT). D'Mello *et al.* [37] proposed an angled polarization splitter in SOI with specially-designed input and output waveguides connected to an MMI region. Another approach is an angled-MMI (AMMI) structure, which has been used widely to realize compact and broadband wavelength division multiplexers and de-multiplexers [37–40]. Recently, Liang *et al.* proposed a compact PS design in SOI based on an AMMI structure [41], which is attractive because of the smaller footprint (~ 30 μm×5 μm) and broad operational bandwidth of 53 nm with an extinction ratio (ER)>20 dB.

These demonstrations in silicon have been more challenging to implement in a small-footprint SiN device, due to the lower refractive index and birefringence of SiN waveguides. In this work, we use the concept of self-imaging in an AMMI, but with major design variations, to demonstrate an ultra-broadband PS in a SiN integrated photonics platform. Our fabricated device shows a bandwidth of >100 nm (over C+L band) with CT less than −18 dB and −20 dB for both TE and TM polarizations. Moreover, the device has a small footprint ~ 80 μm×13 μm, and we demonstrate significant tolerance of fabrication variation. We also show that the device works as a polarization combiner (PC) in the reverse direction. The IL of the splitter/combiner is measured to be ~ 0.7 dB for TE and ~ 0.8 dB for TM polarizations. Although there have been prior experimental demonstrations of integrated optical polarization splitters, using a variety of materials and operating principles [34,35,37], the approach described here provides a unique combination of small footprint, wide optical bandwidth, and simple fabrication. We discuss the detailed device design principles in Section 2 and present experimental results in Section 3.

2. Design and simulation

A 3D schematic illustration of our proposed AMMI PS is shown in Fig. 1(a). We use the standard nomenclature to describe the two orthogonal polarizations, "TE" refers to the quasi-TE mode in which the horizontal field component E_y is dominant, while "TM" refers to the quasi-TM mode in which the vertical (E_z) field component is dominant. The device splits the TE- and TM-polarizations launched at the IN-port to output ports OUT1 and OUT2 respectively, as indicated in the figure. A SEM image of the fabricated AMMI PS is also shown in the inset. The top-view and cross-section of the device with design parameters are shown in Fig. 1(b). The device is designed on a 450-nm thick (h) SiN (n_{SiN} = 1.9973) on SiO_2 $\left(n_{\mathrm{SiO_2}} = 1.455\right)$ waveguides with 2.5 μm SiO_2 cladding (t_{BOX} = 2.5 μm). The input waveguide connects to the multimode waveguide on one side at angle θ_1. Similarly, the TE-output waveguide connects to the multimode waveguide on the same side at an angle θ_2 and at a distance L_1 from the input port. The MMI waveguide is tapered to a single-mode TM output port over a length L_2. W_1 is the width of input and output single-mode waveguides and W_2 is the width of the multimode waveguide.

Optics EXPRESS

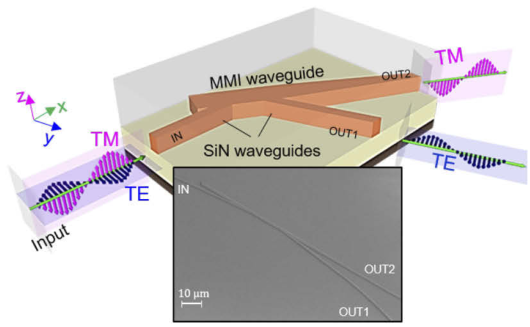

(a) (b)

Fig. 1. Schematics of the proposed AMMI PS; (a) 3D view with a SEM image of the fabricated device in inset, (b) top-view and cross-section with design parameters.

In a conventional MMI coupler, a large number of modes travelling with different propagation constants interfere and form self-images of the input field distribution at every $3L_\pi$. The beat length L_π is defined as [42]:

$$L_\pi = \frac{\pi}{\beta_0 - \beta_1} \approx \frac{4n_{\text{eff},0}W_2^2}{3\lambda}, \tag{1}$$

where $\beta_0 = 2\pi n_{\text{eff},0}/\lambda$ and $\beta_1 = 2\pi n_{\text{eff},1}/\lambda$ are the propagation constants of the fundamental ($m = 0$) and first order ($m = 1$) modes respectively, and $n_{\text{eff},0}$ is the effective index of fundamental mode. For a multimode waveguide with $\Delta n_{\text{eff}}^{\text{TE}} \neq \Delta n_{\text{eff}}^{\text{TM}}$ (where $\Delta n_{\text{eff}} = n_{\text{eff},0} - n_{\text{eff},1}$) the self-image patterns of TE and TM polarizations (at any operating λ) are different. This means that the MMI (polarization splitting) length is different for both polarizations. Thus, in a conventional MMI-based PS, effectively positioning the output ports at same MMI length is challenging. To minimize the CT between the output ports, various design approaches have been reported in [36,37]. As an alternative, angled multimode structures offer superior device performance (IL, CT, etc) and relaxed fabrication requirements when compared to conventional (straight) MMIs [30,39]. We base our design for a SiN PS on this concept.

We performed a series of 3D finite difference time domain (FDTD) simulations to optimize the device parameters for maximum performance in-terms of CT, IL and bandwidth. First, we selected the widths of the single-mode waveguides (W_1) and the MMI waveguide (W_2). We calculated the number of guided modes and their n_{eff} as a function of waveguide width W, as shown in Fig. 2(a). These simulations were carried out using the finite-difference eigenmode method at $\lambda = 1550$ nm and $h = 450$ nm. The width of the multimode waveguide is chosen to support only the two lowest order modes for both the polarizations, as indicated by the shaded region 1 µm<W_2<1.75 µm in Fig. 2(a). Wider multimode waveguides (beyond 1.75 µm) introduce phase error due to the excitation of higher order modes, which leads to dispersive self-imaging [43,44]. In order to achieve a high mode index contrast ($n_{\text{eff},0} - n_{\text{eff},1}$) and correspondingly short device length ($L_1 \propto L_\pi^{\text{TE}} \propto W_2^2$), we choose $W_2 \sim 1.25$ µm. The width of the single mode waveguide is fixed at $W_1 = 900$ nm. A wider input waveguide reduces the IL at the input-MMI interface [45,46].

Next, we model the distance between the input and TE output waveguides (L_1) as a function of the input waveguide angle (θ_1). Keeping $W_1 = 900$ nm and $W_2 = 1.25$ µm, we simulated a long AMMI without output ports using 3D FDTD for different values of θ_1. As an example, Fig. 2(b) illustrates the simulated interference pattern of an AMMI ($\theta_1 = 5$ °) for input TE (top) and TM (bottom) polarizations, at $\lambda = 1550$ nm. A series of peaks and nulls are observed along the edges of the MMI in both the cases. Due to the different propagation constants of the TE and TM polarization, the peaks (nulls) for TE and nulls (peak) for TM coincide at some points, marked as

Optics EXPRESS

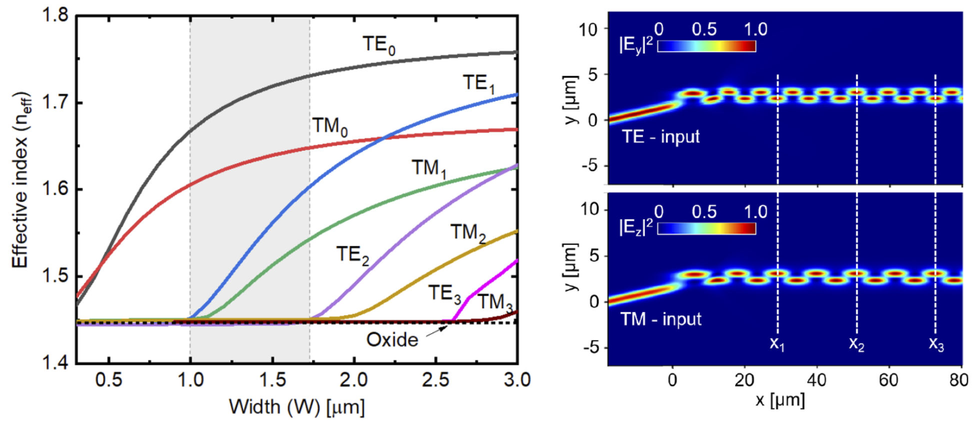

(a) (b)

Fig. 2. (a) Effective indices (n_{eff}) of supported modes as a function of waveguide width (W) calculated at λ = 1550 nm and for fixed h = 450 nm. (b) The interference patterns of a long AMMI (W_1 = 900 nm, W_2 = 1.25 µm, θ_1 = 5 deg) without output ports simulated in 3D FDTD at λ = 1550 nm, for TE (top) and TM (bottom) inputs. x_1, x_2, and x_3 represent the locations where a peak (null) of propagating TE mode and a null (peak) of the propagating TM mode coincides.

x_1, x_2, x_3. In order to minimize the device footprint, we select the closest point x_1 as the location of TE-output waveguide.

Figure 3(a) shows the distance between the input and TE output waveguides L_1 as a function of θ_1 for W_2 = 1.25 µm and W_2 = 1.5 µm. The position of x_1 (and L_1) is dependent on the input waveguide angle θ_1. At one extreme, as $\theta_1 \to 0$, the AMMI works like a conventional MMI, with the images moving away from the sidewalls. The contrast and clarity of the patterns along the edges of the AMMI improve as θ_1 increases. Simultaneously, the length L_1 increases with θ_1 and W_2. For the rest of the calculations we fixed W_2 = 1.25 µm which corresponds to $L_1 \sim 20$ µm for the given range of θ_1 (3 °<θ_1<9 °).

To optimize the θ_1 and θ_2, we simulate the AMMI structure with the TE-output connected at L_1 (a function of θ_1) as in Fig. 3(a). We then set $\theta_1 = \theta_2$ and simulate the transmission at OUT1 (P_1^{TE}) while exciting the input with a TE-polarized source.

As shown in Fig. 3(b), the TE-transmission to OUT1 (P_1/P_{in}) is maximum when 5 ° $\leq \theta_{1,2} \leq$ 7 °. For θ_2<5 °, the transmission decreases as the power couples back to the MMI waveguide, as indicated by the increase in P_2^{TE} . Also, for θ_2>7 °, the loss becomes significant due to radiation leakages (radiation loss, RL) at the input/MMI and MMI/output interface. To balance the needs for smaller footprint (shorter L_1) and low CT, we set θ_1 = 5 ° (smaller L_1) and θ_2 = 7 °.

Finally, we repeated these simulations for a TM-polarized input after connecting a taper of length L_2 between the MMI (W_2 = 1.25 µm) and OUT2 (W_1 = 900 nm). The optimum taper-length for maximum output power P_2 is ~ 35 µm. The transmission (P_2/P_{in}) and radiation loss ($(P_1 + P_2)/P_{\text{in}}$) for a TM-input is also shown in Fig. 3(b). The 3D-FDTD simulations of our AMMI PS with optimized design parameters (W_1 = 900 nm, W_2 = 1.25 µm, θ_1 = 5 °, L_1 = 20.85 µm, θ_2 = 7 ° and L_2 = 35 µm) for TE-input and TM-input at $\lambda \sim$ 1550 nm are shown in Fig. 4(a) and 4(b) respectively.We further investigated the spectral response of the optimized AMMI PS. In the previous discussion, the length L_1 (= 20.85 µm) is optimized at λ = 1550 nm. However, $L_1(\propto L_\pi)$ must change with respect to λ. Since the higher order modes in the MMI waveguide

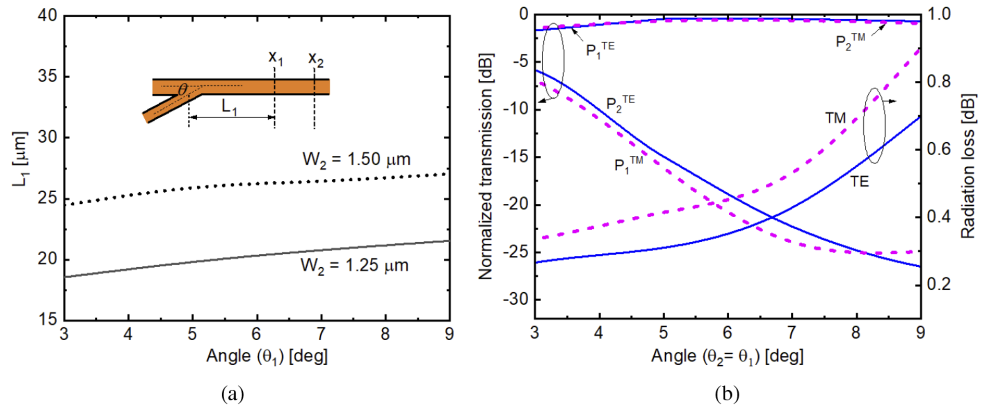

Fig. 3. (a) The distance L_1 in Fig. 1(b) (location of x_1 in Fig. 2(b)) simulated as a function of θ_1 for $W_2 = 1.25$ μm and $W_2 = 1.5$ μm. (b) The transmission ($P_{1,2}/P_{in}$) and radiation loss ($(P_1 + P_2)/P_{in}$) at the output ports for various tilt angles, $\theta_1 = \theta_2$ calculated using FDTD simulation of the complete device ($W_1 = 900$ nm, $W_2 = 1.25$ μm, $\lambda = 1550$ nm). The angle for maximum TE-output (P_1) is first optimized without considering the taper between the MMI and TM-output port.

are suppressed by choosing $W_2 = 1.25$ μm, L_1 can be approximately expressed as,

$$L_1(\lambda) \approx \frac{L_\pi^{TE}(\lambda) \times L_\pi^{TM}(\lambda)}{|L_\pi^{TE}(\lambda) - L_\pi^{TM}(\lambda)|}, \tag{2}$$

where $L_\pi(\lambda) = \lambda/\Delta n_{eff}(\lambda)$, from Eq. (1). Thus, we designed the MMI for nearly wavelength independent operation such that $dL_1(\lambda)/d\lambda \sim 0$ in the 1525 nm$\leq \lambda \leq$ 1625 nm. Figure 5(a) shows the calculated L_πs and L_1 over the C+L band for both TE and TM polarizations. Both L_π^{TE} and L_π^{TM} have some wavelength dependence, however, the corresponding L_1 is nearly wavelength independent over the C+L band. The change in L_1 (ΔL_1) is +200 nm to −700 nm within the 1525 nm to 1625 nm wavelength window ($\Delta L_1 = 0$ at $\lambda = 1550$ nm). Note that the value of L_1 (20.31 μm) calculated using Eq. (2) is nearly equal to that from FDTD simulation (20.85 μm). The inset of the figure shows the calculations in 1400 nm to 1800 nm wavelength span. Significant wavelength dependence is observed at higher wavelengths since the slope of L_π^{TM} and L_π^{TE} increases for λ>1750 nm. Also, we expect wavelength dependence for λ<1480 nm since the MMI waveguide supports additional modes (>2) in this regime. The simulated wavelength dependent transmission characteristics of the optimized device in the C+L band are shown in Fig. 5(b). The CT between the outputs is calculated to be < -17 dB and < -18 dB for TE and TM polarizations, respectively. The inset shows a coarse simulation of the spectral response in 1400 nm$\leq \lambda \leq$ 1800 nm. As expected, the CT increases (exceeding -15 dB) for $\lambda \lesssim 1490$ nm and for $\lambda \gtrsim 1700$ nm.

Tolerance to fabrication variations is an important aspect of this structure, and the most likely fabrication errors are in the waveguide widths W_1 and W_2. Small changes in either of these widths most directly affect the polarization beat length, and thus the ideal value of L_1. Thus, we can use a change in L_1 (ΔL_1) as a single-variable proxy for variations in W_1 and W_2. Figure 6(a) shows that the CT for both polarizations ($CT^{TE} = P_1^{TM}/P_{in}^{TM}$, $CT^{TM} = P_2^{TE}/P_{in}^{TE}$) is not expected to exceed −15 dB for $|\Delta L_1|$<500 nm. In Fig. 6(b), we map this L_1 variation to corresponding window of waveguide width (W) variations. For example, $|\Delta W| \lesssim 45$ nm, the ideal L_1 would change by <500 nm, and the CT would remain below -15 dB.

The proposed AMMI PS also works as a polarization combiner (PC) in the reverse direction. Figure 7(a) shows the simulation results with TE-input at OUT1 port (top) and TM-input at

Optics EXPRESS

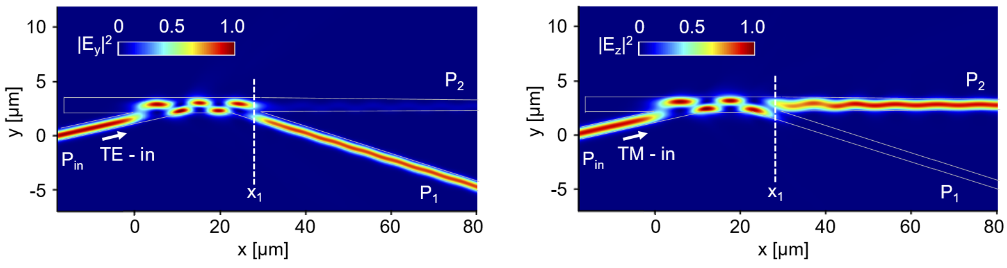

Fig. 4. 3D FDTD simulation of AMMI PS for (a) TE-input and (b) TM-input at λ = 1550 nm. The optimized device parameters are W_1 = 900 nm, W_2 = 1.25 μm, θ_1 = 5 deg, θ_2 = 7 deg, L_1 = 20.85 μm and L_2 = 35 μm.

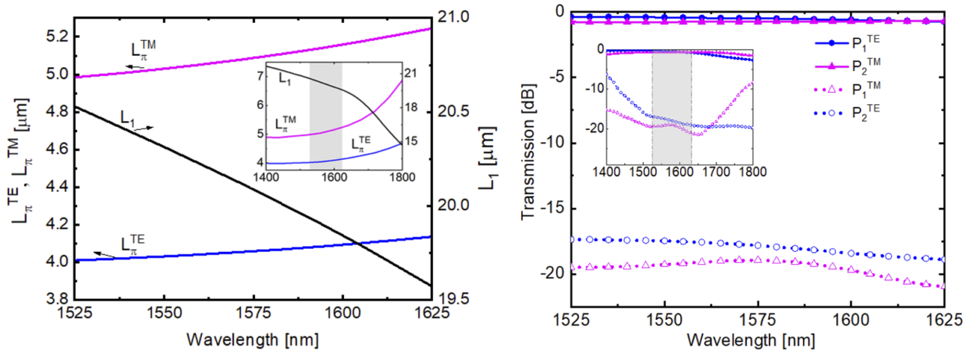

Fig. 5. (a) Wavelength dependent L_π^{TE}, L_π^{TM} and ΔL_1 (using Eq. (2)) calculated over C+L band, for W_2 = 1.25 μm. (b) Normalized transmission at the TE- and TM- output ports for both polarizations.

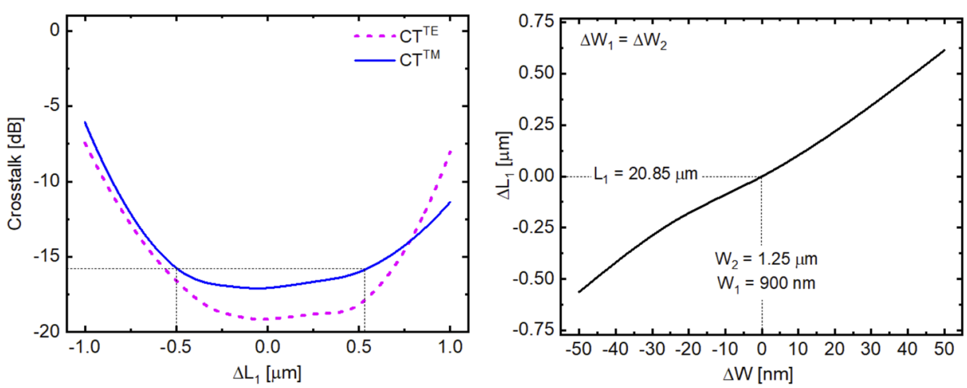

Fig. 6. Tolerance to the parameter variations for the device in Fig. 4; (a) CT versus ΔL_1 calculated at TE-output port ($CT^{TE} = P_1^{TM}/P_{in}^{TM}$) and TM-output port ($CT^{TM} = P_2^{TE}/P_{in}^{TE}$); (b) ΔL_1 (L_1 = 20.85 μm) with respect to $\Delta W = \Delta W_1 = \Delta W_2$ (at ΔW = 0, W_1 = 900 nm and W_2 = 1.25 μm).

Optics EXPRESS

OUT2 port (bottom). This means that when both OUT1 and OUT2 are excited with TE and TM sources, respectively, they will be combined at port IN. Interestingly, for a TE-polarized excitation at OUT2 and TM-polarized excitation at OUT1, the inputs will not be combined at port IN, but rather at the MMI input-end, where the waveguide is terminated, as shown in Fig. 7(b). Figure 8(a) shows the FDTD simulation of the electric field profile of a cascaded PS and PC for TE and TM inputs. The absence of spectral interference fringes in Fig. 8(b) indicates negligible interference between the two arms.

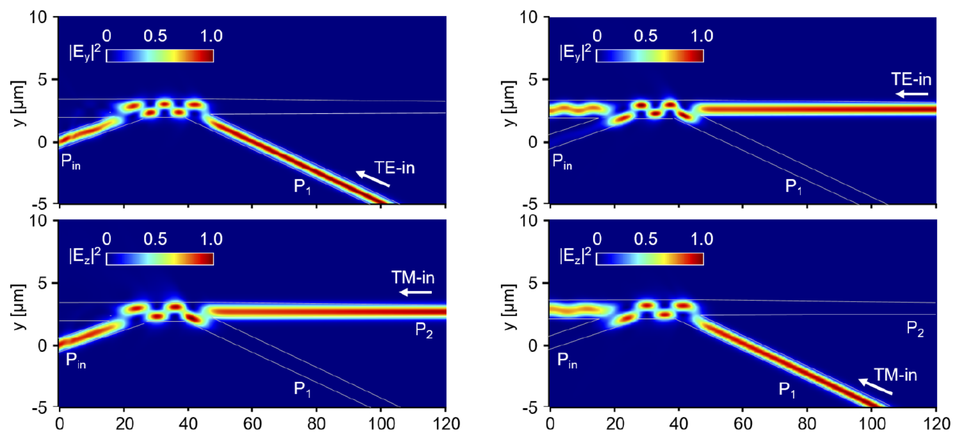

(a) (b)

Fig. 7. 3D FDTD simulation of AMMI PS as PC. (a) TE-input at OUT1 port (top) and TM-input at OUT2 port (bottom). (b) TE-input at OUT2 port (top) and TM-input at OUT1 port (bottom).

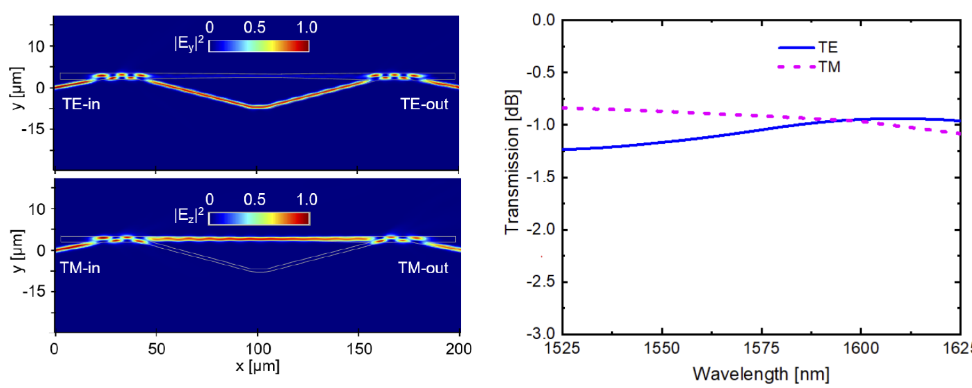

(a) (b)

Fig. 8. 3D FDTD simulation of a cascaded AMMI PS and PC for TE and TM inputs; (a) electric field profile and (b) transmission at the output ports.

3. Experimental demonstration

We fabricate the designed AMMI in 450-nm thick LPCVD SiN on 2.5 μm thick thermal SiO_2. An ellipsometric measurement of the SiN film fits well to the wavelength-dependent refractive index values for stoichiometric amorphous silicon nitride from [47], in which $n_{\mathrm{SiN}}(\lambda \sim 1550\ \mathrm{nm}) =$

Optics EXPRESS

1.9973. We define the pattern using electron-beam lithography (EBL) and inductively-coupled plasma reactive ion etching (ICPRIE). Finally, we deposit 2.5 μm PECVD SiO_2 top cladding. Figure 9(a) shows optical microscope images of a fabricated polarization splitter and combiner along with a reference waveguide. A SEM image of the polarization splitter/combiner is shown in

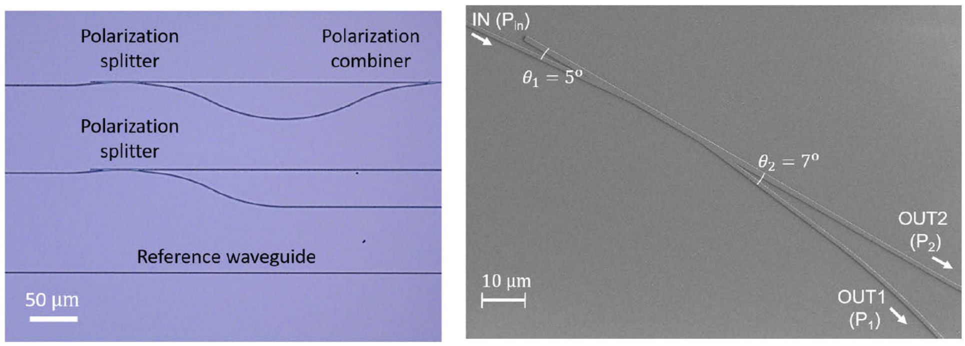

(a) (b)

Fig. 9. (a) Optical microscope image of the fabricated AMMI polarization splitter/combiner along with a reference waveguide. (b) SEM image of the AMMI PS prior to the deposition of SiO_2 top cladding.

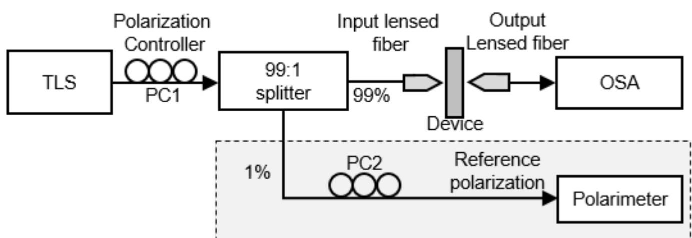

Fig. 10. Optical characterization setup; TLS - tunable laser source, OSA - optical spectrum analyser.

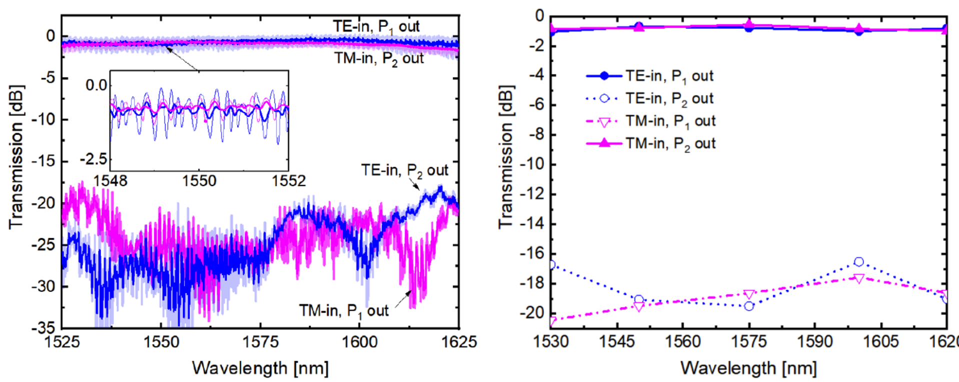

(a) (b)

Fig. 11. Transmission characteristics at the output ports of an AMMI PS; (a) measured using a high resolution (0.8 pm) OSA and internal TLS (P_{in} = 125 μW, 1525 nm≤ λ ≤1625 nm (inset shows the un-averaged and smoothed data near λ = 1550 nm), (b) measured at $P_{\text{in}} \sim 100$ mW using an EDFA amplified TLS and an optical power meter.

Optics EXPRESS

9(b). For better fiber-to-chip coupling efficiency, the input and output waveguides are terminated with inverse tapers (450 nm×450 nm) of length 400 μm, and the end-facets of the chip are polished. The total length of the chip (reference waveguide) is ~ 4 mm.

We characterized the devices by aligning lensed fibers to the inverse-taper edge couplers at the input and output facets. A schematic of the optical characterization setup is shown in Fig. 10. The tunable laser source (TLS) is internal to the optical spectrum analyzer and has a maximum output power of −4.5 dBm over 1525 nm≤ λ ≤1625 nm. Before inserting the chip into the setup, we align the polarimeter to the input lensed fiber and align the polarization to one of the axes (TE or TM) by adjusting the fiber polarization controller PC1. The reference polarization is then set to the same polarization using PC2. Thus, the polarization at the input of device can be aligned to any state (TE or TM) by adjusting PC1 and monitoring the reference polarization.The fiber-to-chip coupling loss of the fabricated devices is estimated to be ~ 4.5 dB (5.3 dB) per facet for TE (TM) polarization, and we define P_{in} to be the power in the waveguide, taking into account this facet loss.

The measured transmission (normalized w.r.t. the reference waveguide) at output ports P_1 and P_2 for both TE and TM inputs is shown in Fig. 11(a). For ease of viewing, we processed this data using a moving average method (0.26 nm) in order to smooth out the small (<1 dB) fringes due to reflections off the chip edge facets. The raw data is also included in a lighter color. Note that the TE and TM outputs are nearly wavelength-independent with IL <1 dB for both the polarizations. The CT is $\lesssim -18$ dB for TE and $\lesssim -19$ dB for TM over the entire wavelength range (1525 nm to 1625 nm) which is consistent with what was expected from numerical simulations. In order to determine the effect of high optical powers on the splitter performance, we tested the performance with an amplified $P_{\text{in}} \sim 100$ mW (a different TLS amplified by an EDFA). The output power (P_1, P_2) is measured using an optical power meter at discrete wavelength points, as shown in Fig. 11(b). Note that, the device performance is nearly wavelength independent with CT $\lesssim -16$ dB and IL <1 dB for TE and TM polarizations.

The fabrication tolerance of the device is estimated experimentally in terms of ΔL_1, which we use as a proxy for variations in W_1 and W_2. Though the length L_1 can be very accurately controlled, any lithographic variation in device parameters W_1 and W_2 will result in a change in the optimal L_1 (see Fig. 6(b)). We fabricated a set of five devices (PS#1 − 5) each with an offset $\Delta L = 0.5$ μm ($L_1 \pm \Delta L_1$) from the design $L_1 = 20.85$ μm. The CT and IL of these devices are measured at $\lambda = 1550$ nm as shown in Fig. 12(b). Error bars represent the fluctuations across the wavelength range. As expected from our calculations in Fig. 6, this data suggests some fabrication tolerance in the design; even for an offset of 500 nm, corresponding to $\Delta W = \Delta W_1 = \Delta W_2 = \pm 45$ nm, CT remains below −10 dB and IL does not significantly change.

We further fabricated a set of cascaded PSs and PCs fabricated on the same sample as shown in the inset in Fig. 13(a). Figure 13(a) shows the transmission at the output of a single cascaded PS and PC (as marked in inset), forming a MZI configuration (the path difference between TE and TM is ~ 16 μm, corresponding to a free spectral range of ~ 73 nm). Since the CT between the TE and TM output ports is negligible (−15 dB) for all wavelengths, the PS output is combined at the output without measurable interference (see Fig. 8). The total IL of this cascaded device is approximately twice that of the PS alone. We further measured the transmission and IL of all other cascaded combinations of PSs and PCs. The wavelength dependent IL (IL^{TE} and IL^{TM}) of a single device (PS or PC) is then estimated by linearly fitting IL with respect to the number of PSs/PCs as shown in Fig. 8, where we assumed identical insertion loss for PSs and PCs . The inset shows the linear fit of IL^{TE} and IL^{TM} versus number of devices measured at $\lambda = 1550$ nm. The excess loss at the input/MMI and MMI/output slightly increases with wavelength, which is expected when the self-images move away from the optimized location L_1. The error bars represent the uncertainty of the slope of the linear fit. This measurement shows that IL^{TE} ranges between 0.6 dB and 0.85 dB and IL^{TM} ranges between 0.74 dB and 0.92 dB across the C+L band.

Research Article | Vol. 28, No. 23 / 9 November 2020 / *Optics Express* 34120

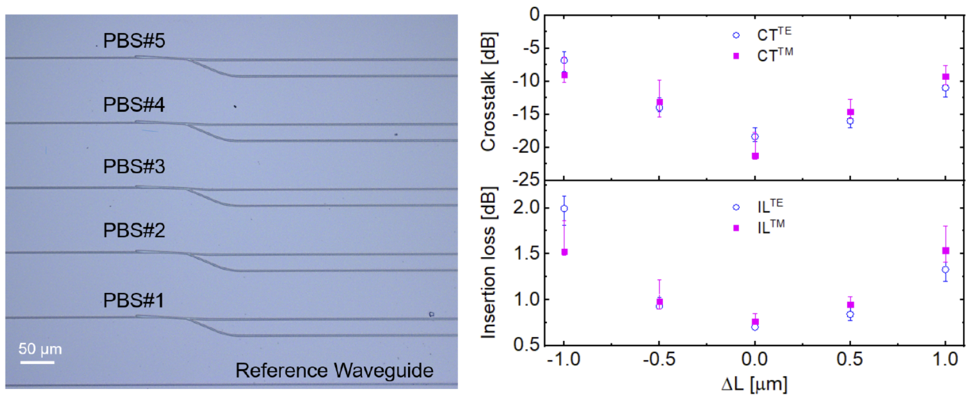

(a) (b)

Fig. 12. (a) Microscope image of a set of five devices (PS#1 − 5) each with an offset $\Delta L_1 = 0.5$ μm ($L_1 \pm \Delta L_1$) from the design $L_1 = 20.85$ μm; (b) IL and CT measured at $\lambda = 1550$ nm for the devices in (a). The error bars represent the fluctuations across the C+L band.

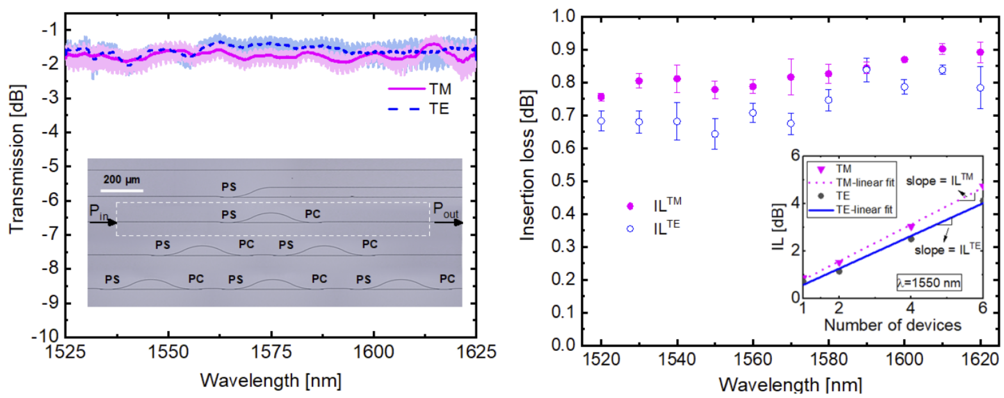

(a) (b)

Fig. 13. (a) Transmission ($P_{\text{out}}/P_{\text{in}}$) characteristics of a single cascaded PS-PC (inset: optical microscope image of a set of cascaded PSs and PCs). (b) Wavelength dependent IL (IL^{TE} and IL^{TM}) of a single PS or PC (assuming identical IL for splitter and combiner) estimated by linearly fitting the IL w.r.t number of PSs/PCs (eg. at $\lambda = 1550$ nm in inset). The error bars represent the uncertainty of the slope of the linear fit.

4. Conclusions

In this work, we reported an AMMI polarization splitter/polarization combiner in a 450-nm thick LPCVD SiN-on-oxide platform. The device design is relatively simple, straightforward and adaptable as compared to that of conventional DC, MMI and MZI based approaches. Moreover, the device fabrication requires a single-layer process. Although we fabricated the device using EBL, feature sizes are generally compatible with deep-UV lithography; the minimum gap between Y-junction waveguides may not resolve as well, but the maximum ΔL_1 would be less than 0.5 μm. This would have little effect on device performance, as shown in the tolerance measurement Fig. 12(b). The device footprint is 80 μm×13 μm which is the smallest PS demonstrated in SiN platform to the best of our knowledge. The measured PS has nearly uniform cross-talk of < -18 dB (< -20 dB) and insertion-loss of ∼ 0.7 dB (∼ 1.0 dB) for TE (TM) polarization over the measured wavelength range of 1525 nm≤ λ ≤1625 nm and beyond and the performance does not change significantly at high input powers. We also demonstrated that the device works as a PC when configured in reverse direction. The measurement results show a good agreement with the simulation results. This design approach is flexible for other device layer heights and compatible with other integrated photonics platforms. Altogether, our AMMI is a good candidate for a PIC foundry-compatible SiN PS and combiner, a critical component for polarization-diversity PICs.

Disclosures

The authors declare no conflicts of interest.

References

1. C. Batten, A. Joshi, J. Orcutt, A. Khilo, B. Moss, C. W. Holzwarth, M. A. Popovic, H. Li, H. I. Smith, J. L. Hoyt, F. Kärtner, R. Ram, V. Stojanović, and K. Asanović, "Building many-core processor-to-DRAM networks with monolithic CMOS silicon photonics," IEEE Micro **29**(4), 8–21 (2009).
2. T. Horikawa, D. Shimura, H. Okayama, S.-H. Jeong, H. Takahashi, J. Ushida, Y. Sobu, A. Shiina, M. Tokushima, K. Kinoshita, and T. Mogami, "A 300-mm silicon photonics platform for large-scale device integration," IEEE J. Sel. Top. Quantum Electron. **24**(4), 1–15 (2018).
3. P. P. Absil, P. Verheyen, P. De Heyn, M. Pantouvaki, G. Lepage, J. De Coster, and J. Van Campenhout, "Silicon photonics integrated circuits: a manufacturing platform for high density, low power optical I/O's," Opt. Express **23**(7), 9369–9378 (2015).
4. F. Boeuf, S. Cremer, E. Temporiti, M. Fere, M. Shaw, C. Baudot, N. Vulliet, T. Pinguet, A. Mekis, G. Masini, H. Petiton, P. L. Maitre, M. Traldi, and L. Maggi, "Silicon photonics R&D and manufacturing on 300-mm wafer platform," J. Lightwave Technol. **34**(2), 286–295 (2016).
5. M. Hochberg and T. Baehr-Jones, "Towards fabless silicon photonics," Nat. Photonics **4**(8), 492–494 (2010).
6. D. Tan, K. Ooi, and D. Ng, "Nonlinear optics on silicon-rich nitride—a high nonlinear figure of merit CMOS platform," Photonics Res. **6**(5), B50–B66 (2018).
7. D. J. Blumenthal, R. Heideman, D. Geuzebroek, A. Leinse, and C. Roeloffzen, "Silicon nitride in silicon photonics," Proc. IEEE **106**(12), 2209–2231 (2018).
8. G. Micó, L. A. Bru, D. Pastor, D. Doménech, J. Fernández, A. Sánchez, J. M. Cirera, C. Domínguez, and P. Muñoz, "Silicon nitride photonics: from visible to mid-infrared wavelengths," in *Silicon Photonics XIII*, vol. 10537 (International Society for Optics and Photonics, 2018), p. 105370B.
9. C. Lacava, S. Stankovic, A. Z. Khokhar, T. D. Bucio, F. Gardes, G. T. Reed, D. J. Richardson, and P. Petropoulos, "Si-rich silicon nitride for nonlinear signal processing applications," Sci. Rep. **7**(1), 22 (2017).
10. M. R. Dizaji, C. J. Krückel, A. Fülöp, P. A. Andrekson, and L. R. Chen, "Silicon-rich nitride waveguides for ultra-broadband nonlinear signal processing," Opt. Express **25**(11), 12100–12108 (2017).
11. C. G. Roeloffzen, L. Zhuang, C. Taddei, A. Leinse, R. G. Heideman, P. W. van Dijk, R. M. Oldenbeuving, D. A. Marpaung, M. Burla, and K.-J. Boller, "Silicon nitride microwave photonic circuits," Opt. Express **21**(19), 22937–22961 (2013).
12. S. Romero-García, F. Merget, F. Zhong, H. Finkelstein, and J. Witzens, "Silicon nitride CMOS-compatible platform for integrated photonics applications at visible wavelengths," Opt. Express **21**(12), 14036–14046 (2013).
13. D. Dai, L. Liu, L. Wosinski, and S. He, "Design and fabrication of ultra-small overlapped AWG demultiplexer based on α-Si nanowire waveguides," Electron. Lett. **42**(7), 400–402 (2006).
14. T. Barwicz, M. R. Watts, M. A. Popović, P. T. Rakich, L. Socci, F. X. Kärtner, E. P. Ippen, and H. I. Smith, "Polarization-transparent microphotonic devices in the strong confinement limit," Nat. Photonics **1**(1), 57–60 (2007).
15. D. Dai, L. Liu, S. Gao, D.-X. Xu, and S. He, "Polarization management for silicon photonic integrated circuits," Laser Photonics Rev. **7**(3), 303–328 (2013).
16. P. Velha, V. Sorianello, M. Preite, G. De Angelis, T. Cassese, A. Bianchi, F. Testa, and M. Romagnoli, "Wide-band polarization controller for Si photonic integrated circuits," Opt. Lett. **41**(24), 5656–5659 (2016).
17. J. Sarmiento-Merenguel, R. Halir, X. Le Roux, C. Alonso-Ramos, L. Vivien, P. Cheben, E. Durán-Valdeiglesias, I. Molina-Fernández, D. Marris-Morini, D.-X. Xu, J. H. Schmid, S. Janz, and A. Ortega-Moñux, "Demonstration of integrated polarization control with a 40 dB range in extinction ratio," Optica **2**(12), 1019–1023 (2015).
18. S. Wang and D. Dai, "Polarization-insensitive 2× 2 thermo-optic Mach–Zehnder switch on silicon," Opt. Lett. **43**(11), 2531–2534 (2018).
19. C. Li, J. H. Song, J. Zhang, H. Zhang, S. Chen, M. Yu, and G. Lo, "Silicon polarization independent microring resonator-based optical tunable filter circuit with fiber assembly," Opt. Express **19**(16), 15429–15437 (2011).
20. H. Fukuda, K. Yamada, T. Tsuchizawa, T. Watanabe, H. Shinojima, and S.-I. Itabashi, "Polarization beam splitter and rotator for polarization-independent silicon photonic circuit," in *2007 4th IEEE International Conference on Group IV Photonics*, (IEEE, 2007), pp. 1–3.
21. H. Fukuda, K. Yamada, T. Tsuchizawa, T. Watanabe, H. Shinojima, and S.-I. Itabashi, "Silicon photonic circuit with polarization diversity," Opt. Express **16**(7), 4872–4880 (2008).

22. Y. Ding, L. Liu, C. Peucheret, and H. Ou, "Fabrication tolerant polarization splitter and rotator based on a tapered directional coupler," Opt. Express **20**(18), 20021–20027 (2012).
23. Y. Xiong, D.-X. Xu, J. H. Schmid, P. Cheben, S. Janz, and N. Y. Winnie, "Fabrication tolerant and broadband polarization splitter and rotator based on a taper-etched directional coupler," Opt. Express **22**(14), 17458–17465 (2014).
24. D. Dai and J. E. Bowers, "Novel concept for ultracompact polarization splitter-rotator based on silicon nanowires," Opt. Express **19**(11), 10940–10949 (2011).
25. Y. Zhang, Y. He, X. Jiang, B. Liu, C. Qiu, Y. Su, and R. A. Soref, "Ultra-compact and highly efficient silicon polarization splitter and rotator," APL Photonics **1**(9), 091304 (2016).
26. Y. Ma, Y. Liu, H. Guan, A. Gazman, Q. Li, R. Ding, Y. Li, K. Bergman, T. Baehr-Jones, and M. Hochberg, "Symmetrical polarization splitter/rotator design and application in a polarization insensitive WDM receiver," Opt. Express **23**(12), 16052–16062 (2015).
27. Y. Zhao, C. Qiu, A. Wu, H. Huang, J. Li, Z. Sheng, W. Li, X. Wang, and F. Gan, "Broadband polarization splitter-rotator and the application in WDM receiver," IEEE Photonics J. **11**(1), 1–10 (2019).
28. X. Chen, C. Qiu, Z. Sheng, A. Wu, H. Huang, Y. Zhao, W. Li, X. Wang, S. Zou, and F. Gan, "Design of an ultra-broadband and fabrication-tolerant silicon polarization rotator splitter with SiO_2 top cladding," Chin. Opt. Lett. **14**(8), 081301 (2016).
29. W. D. Sacher, Y. Huang, L. Ding, T. Barwicz, J. C. Mikkelsen, B. J. Taylor, G.-Q. Lo, and J. K. Poon, "Polarization rotator-splitters and controllers in a Si_3N_4-on-SOI integrated photonics platform," Opt. Express **22**(9), 11167–11174 (2014).
30. H. Liang, R. Soref, J. Mu, X. Li, and W.-P. Huang, "Electro-optical phase-change 2×2 switching using three-and four-waveguide directional couplers," Appl. Opt. **54**(19), 5897–5902 (2015).
31. Z. Lu, Y. Wang, F. Zhang, N. A. Jaeger, and L. Chrostowski, "Wideband silicon photonic polarization beamsplitter based on point-symmetric cascaded broadband couplers," Opt. Express **23**(23), 29413–29422 (2015).
32. D. Dai and J. E. Bowers, "Novel ultra-short and ultra-broadband polarization beam splitter based on a bent directional coupler," Opt. Express **19**(19), 18614–18620 (2011).
33. H. Wu, Y. Tan, and D. Dai, "Ultra-broadband high-performance polarizing beam splitter on silicon," Opt. Express **25**(6), 6069–6075 (2017).
34. S. Gao, Y. Wang, K. Wang, and E. Skafidas, "Low-loss and broadband 2×2 polarization beam splitter based on silicon nitride platform," IEEE Photonics Technol. Lett. **28**(18), 1936–1939 (2016).
35. S. Guerber, C. Alonso-Ramos, D. Benedikovic, E. Durán-Valdeiglesias, X. Le Roux, N. Vulliet, E. Cassan, D. Marris-Morini, C. Baudot, F. Boeuf, and L. Vivien, "Broadband polarization beam splitter on a silicon nitride platform for o-band operation," IEEE Photonics Technol. Lett. **30**(19), 1679–1682 (2018).
36. M. Yin, W. Yang, Y. Li, X. Wang, and H. Li, "CMOS-compatible and fabrication-tolerant MMI-based polarization beam splitter," Opt. Commun. **335**, 48–52 (2015).
37. Y. D'Mello, E. El-Fiky, J. Skoric, A. Kumar, M. Hui, Y. Wang, L. Guenin, D. Patel, and D. V. Plant, "Compact, angled polarization splitter: Characterization of broadband performance and fabrication tolerance," IEEE Photonics J. **10**(6), 1 (2018).
38. J. H. Song, T. D. Kongnyuy, N. Hosseini, P. Neutens, F. Buja, R. Jansen, and X. Rottenberg, "Angled-MMI-based wavelength splitters on silicon nitride waveguide platforms for fluorescence sensing," Appl. Opt. **56**(29), 8055–8060 (2017).
39. Y. Hu, R. Jenkins, F. Gardes, E. Finlayson, G. Mashanovich, and G. Reed, "Wavelength division (de) multiplexing based on dispersive self-imaging," Opt. Lett. **36**(23), 4488–4490 (2011).
40. Y. Hu, F. Gardes, D. Thomson, G. Mashanovich, and G. Reed, "Coarse wavelength division (de) multiplexer using an interleaved angled multimode interferometer structure," Appl. Phys. Lett. **102**(25), 251116 (2013).
41. H. Liang, R. Soref, and J. Mu, "Compact polarization splitter based on a silicon angled multimode interferometer structure," Appl. Opt. **58**(15), 4070–4074 (2019).
42. L. B. Soldano and E. C. Pennings, "Optical multi-mode interference devices based on self-imaging: principles and applications," J. Lightwave Technol. **13**(4), 615–627 (1995).
43. S. Amin, M. Uzma, and T. Azfar, "Investigation of self-imaging position dependence on relative modal phase shifts in MMI waveguides," in *8th International Conference on High-capacity Optical Networks and Emerging Technologies*, (IEEE, 2011), pp. 381–386.
44. A. Maese-Novo, R. Halir, S. Romero-García, D. Pérez-Galacho, L. Zavargo-Peche, A. Ortega-Moñux, I. Molina-Fernández, J. Wangüemert-Pérez, and P. Cheben, "Wavelength independent multimode interference coupler," Opt. Express **21**(6), 7033–7040 (2013).
45. A. Hosseini, H. Subbaraman, D. Kwong, Y. Zhang, and R. T. Chen, "Optimum access waveguide width for $1\times n$ multimode interference couplers on silicon nanomembrane," Opt. Lett. **35**(17), 2864–2866 (2010).
46. D. Thomson, Y. Hu, G. Reed, and J.-M. Fedeli, "Low loss MMI couplers for high performance MZI modulators," IEEE Photonics Technol. Lett. **22**(20), 1485–1487 (2010).
47. E. D. Palik, *Handbook of optical constants of solids*, vol. 1 (Elsevier, 2012).